

See discussions, stats, and author profiles for this publication at: <https://www.researchgate.net/publication/50224702>

Compact pnCCD-Based X-ray Camera with High Spatial and Energy Resolution: A Color X-ray Camera

ARTICLE in ANALYTICAL CHEMISTRY · FEBRUARY 2011

Impact Factor: 5.64 · DOI: 10.1021/ac102811p · Source: PubMed

CITATIONS

44

READS

52

21 AUTHORS, INCLUDING:



Sebastian Ihle

PNSensor GmbH

16 PUBLICATIONS 103 CITATIONS

[SEE PROFILE](#)



Robert Hartmann

PNSensor GmbH

258 PUBLICATIONS 4,426 CITATIONS

[SEE PROFILE](#)



Markus Kuehbacher

49 PUBLICATIONS 641 CITATIONS

[SEE PROFILE](#)



Reiner Wedell

Institut für angewandte Photonik e.V.

76 PUBLICATIONS 887 CITATIONS

[SEE PROFILE](#)

Compact pnCCD-Based X-ray Camera with High Spatial and Energy Resolution: A Color X-ray Camera

O. Scharf,^{*,†} S. Ihle,[‡] I. Ordavo,[§] V. Arkadiev,^{||} A. Bjeoumikhov,[⊥] S. Bjeoumikhova,[⊥] G. Buzanich,[†] R. Gubzhokov,[⊥] A. Günther,[⊥] R. Hartmann,[‡] M. Kühbacher,[⊗] M. Lang,[‡] N. Langhoff,[⊥] A. Liebel,[§] M. Radtke,[†] U. Reinholtz,[†] H. Riesemeier,[†] H. Soltau,[‡] L. Strüder,^{○,♯} A. F. Thünemann,[†] and R. Wedell^{||}

[†]BAM Federal Institute for Materials Research and Testing, Richard-Willstätter-Strasse 11, 12489 Berlin, Germany,

[‡]PNSensor GmbH, Römerstrasse 28, 80803 München, Germany,

[§]PNDetector GmbH, Emil-Nolde-Strasse 10, 81735 München, Germany,

^{||}Institut für Angewandte Photonik e.V. (IAP), Rudower Chaussee 29/31, 12489 Berlin, Germany,

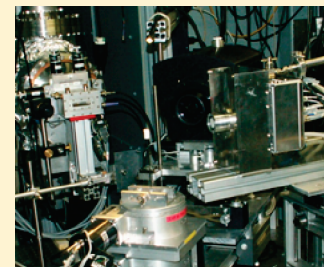
[⊥]IfG-Institute for Scientific Instruments GmbH, Rudower Chaussee 29/31, 12489 Berlin, Germany,

[⊗]Helmholtz Centre Berlin for Materials and Energy, Hahn-Meitner-Platz 1, 14109 Berlin, Germany, and

[○]Max-Planck-Institut für Extraterrestrische Physik, Giessenbachstrasse, 85748 Garching, Germany

[#]Max-Planck-Institut Halbleiterlabor, Otto-Hahn-Ring 6, 81739 München, Germany

ABSTRACT: For many applications there is a requirement for nondestructive analytical investigation of the elemental distribution in a sample. With the improvement of X-ray optics and spectroscopic X-ray imagers, full field X-ray fluorescence (FF-XRF) methods are feasible. A new device for high-resolution X-ray imaging, an energy and spatial resolving X-ray camera, is presented. The basic idea behind this so-called “color X-ray camera” (CXC) is to combine an energy dispersive array detector for X-rays, in this case a pnCCD, with polycapillary optics. Imaging is achieved using multiframe recording of the energy and the point of impact of single photons. The camera was tested using a laboratory 30 μm microfocus X-ray tube and synchrotron radiation from BESSY II at the BAMline facility. These experiments demonstrate the suitability of the camera for X-ray fluorescence analytics. The camera simultaneously records 69 696 spectra with an energy resolution of 152 eV for manganese K α with a spatial resolution of 50 μm over an imaging area of 12.7 \times 12.7 mm². It is sensitive to photons in the energy region between 3 and 40 keV, limited by a 50 μm beryllium window, and the sensitive thickness of 450 μm of the chip. Online preview of the sample is possible as the software updates the sums of the counts for certain energy channel ranges during the measurement and displays 2-D false-color maps as well as spectra of selected regions. The complete data cube of 264 \times 264 spectra is saved for further qualitative and quantitative processing.



Because of ongoing development of X-ray optics and detection systems, X-ray fluorescence (XRF) evolved from selected area element analysis toward spatial resolved elemental imaging.¹ In conventional approaches, a sample is mapped by an X-ray beam. The fluorescence of each mapping position (pixel) is analyzed for the elemental composition using a fine mechanical XYZ-stage. During the last 20 years, there has been a tendency to cross over from compact 1-D detectors to spatial resolving detectors. Most of these detection systems can measure spatial information and the intensity at a pixel size without energy resolution.² Alfeld et al.³ performed the first attempt of fullfield X-ray fluorescence with polycapillary optics and a charge-coupled device (CCD).

IfG Institute for Scientific Instruments GmbH, the BAM Federal Institute for Materials Research and Testing, PNSensor GmbH, and the Institut für Angewandte Photonik e.V. (IAP) have developed and tested a compact camera that combines a spatial and spectral resolving pnCCD⁴ with a polycapillary optics⁵ to a color X-ray camera system with high quantum efficiency and throughput.

The specific pnCCD detector designed for ultrafast readout takes the center stage of the color X-ray camera. This CCD was originally developed at the Halbleiterlabor of the Max-Planck Society as a spectroscopic X-ray imager for the astrophysical satellite mission XMM-Newton.^{6,7} Since that time, continuous development has made this detector very attractive for many other applications, such as imaging of high energy electrons,⁸ energy-resolved two-dimensional X-ray diffraction (XRD)⁹ and synchrotron scattering experiments.¹⁰ The outstanding properties of the pnCCD are, besides its radiation hardness, its high quantum efficiency in the X-ray range, its excellent energy resolution, and its high frame rate capability.

For imaging purposes, the CCD is coupled to polycapillary optics to perform fullfield XRF imaging. The technologies available at the IFG GmbH Company allow the design and manufacture of optimized straight polycapillary structures for 1:1

Received: October 26, 2010

Accepted: February 1, 2011

Published: February 28, 2011

Table 1. Summary of pnCCD Characteristics and Settings

parameter	value
pnCCD type	column-parallel, split frame readout
pixel size	$48 \times 48 \mu\text{m}^2$
number of pixels	69 696
image area	$12.7 \times 12.7 \text{ mm}^2$
sensitive depth	$450 \mu\text{m}$
frame rate	400 Hz (up to 1 kHz possible for specific applications, not used here)
pixel readout speed	28 Mpixel/s
quantum efficiency	>95% at 3 keV – 10 keV; >30% at 20 keV
readout noise (rms)	<3e ⁻ /pixel
charge transfer efficiency	>0.999 95

images as well as of conical polycapillary structures for magnification and demagnification imaging. The camera objective design allows a rapid changing of the X-ray lenses.

■ EXPERIMENTAL SECTION

pnCCD within the Camera Head. The functional concept of the pnCCD is based on the principle of sideward depletion of high resistivity silicon.¹¹ Full depletion of the device volume is achieved, hence making the entire detector thickness of 450 μm sensitive to radiation. A homogeneous and unstructured thin p-implant located on the back side of the device acts as the radiation entrance window (backside illumination). An X-ray entering from the rear interacts with the silicon bulk and creating a certain number of electron–hole pairs. As a result of the strong electric fields in the pnCCD, electrons are separated from holes with the latter drifting to the rear, where they are absorbed by the negative contact. Signal electrons drift toward the front and are confined in the potential minima of the single pixels at a depth of 8 μm . During charge transfer, electrons are transported to the neighboring pixel with minimal losses (charge transfer efficiency >0.999 95). At the end of each CCD line, an integrated JFET amplifier operated as the source follower provides the first signal amplification of the charge signals. Further processing is performed by an ASIC (CMOS amplifier and multiplexer, CAMEX¹²) wire-bonded to the output of each JFET.

An energy resolution better than 152 eV at the manganese K α line (5898.75 eV¹³) for all recombined events is typical (see section Data Analysis).

Because of the detector's sensitive thickness of 450 μm , the quantum efficiency is above 95% in the range from 3 to 10 keV and is around 37% at 20 keV. Moreover, radiation hardness up to 10^{14} photons/cm² at 10 keV has been measured for pnCCDs with no increase in leakage current or readout noise. A high frame rate of 400 Hz (28 Mpixel/s) is obtained due to the channel parallel readout and the split frame operation. At this frame rate, the readout noise is still very low amounting to less than 3e⁻ per pixel rms. The pnCCD inside the CXC has an image area of $12.7 \times 12.7 \text{ mm}^2$ comprising 264 \times 264 pixel with a size of 48 μm ; therefore, split events will occur with high probability (see section of Count Rates).

The main characteristics of the pnCCD used for this application are summarized in the Table 1. A detailed description of the pnCCD within the CXC is presented in another paper.¹⁴

Camera Housing and Cooling. The pnCCD is enclosed in a vacuum sealed camera housing with a mounting flange, which provides the mechanical interface for the polycapillary optics.

The detector is located at 6.2 mm behind the camera entrance window, which consists of a 50 μm thick beryllium foil. For optimal performance, the pnCCD is cooled to a temperature of below -25°C . At this temperature the noise contribution due to dark current is insignificant at the readout speed of 400 Hz. Two double-stage thermoelectric modules (TEC), each with 31 W of cooling power, are used to cool the detector. The heat on the warm sides of the TECs is dissipated by cooling water with a temperature of 5 $^\circ\text{C}$. To suppress humidity condensation at the cold detector surface, the camera head is thermally decoupled from its surrounding by vacuum.

Electronic and Data Acquisition System. The power supplies, the sequencer, and the data acquisition system are located in a 19 in. rack-mount. The voltages for operating the camera head are applied by a computer. The digital pulses and clocks for the ADC boards, the CAMEX chips, and the pnCCD are generated by a sequencer. Details are presented in Ordavo et al.¹⁴ The four analog signal outputs of the detector are processed in parallel by four ADCs on two boards with 14 bit resolution. The digitized data is transmitted by an optical fiber connection to the measurement computer where the data is processed by the software.

The user can select the amplifier bandwidth and the analog gain. A gain optimization for maximum dynamic range at energies up to 10, 15, 20, and 40 keV was applied, respectively.

X-ray Optics for the Camera. An image of an object is formed by the position-sensitive detector which registers individual photons coming to separate pixels. Without optics there is just spatial resolution for X-ray absorption measurements. For X-ray fluorescence, spatial resolution on a sample can be achieved by complementing the detector with special X-ray optics which “guides” photons from small regions on a sample to corresponding pixels on the detector.

For the X-ray color camera, polycapillary optics are used containing a large number of straight channels with diameters in the range for obtaining a 1:1 image on the detector. The transparency of the polycapillary is typically in the order of 75–80% which ensures acceptable intensity losses at the entrance of the CXC. Such high-performance microstructured glass is a product of intensive technological research and development of many years at the Institute for Scientific Instruments.⁵

We assume for simplicity that the spatial resolution of the pnCCD is identical to its pixel size, although subpixel resolution is possible (see section on the Data Analysis). The resulting spatial resolution of the camera remains the same if the channel diameter does not exceed the pixel size. Beam divergence at the entrance and at the exit of channels leads to certain image

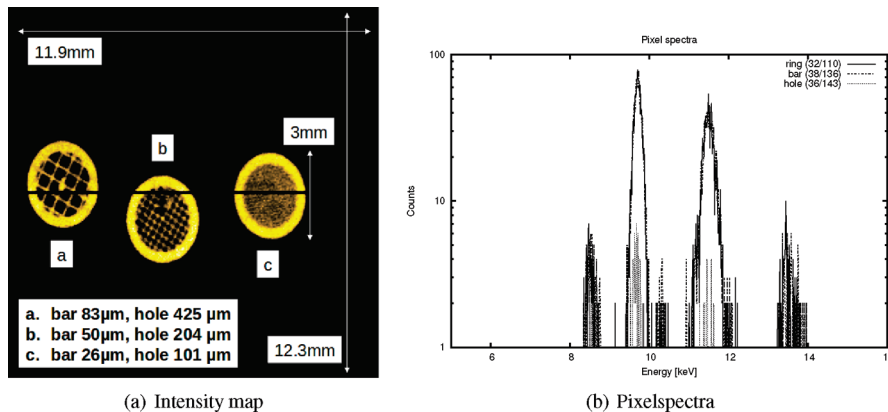


Figure 1. Test object excited by a Rh-microfocus tube, measurement time 20 min. (a) Fullfield view of the camera with three goldmeshes, each 3 mm in diameter. A map of the intensities of the gold L-peak at 9.713 keV is shown. (b) Spectra for three selected pixels: on the ring, on the bar, and on a hole.

spreading. The contribution of beam spreading can be minimized by reducing the distances of sample—optics and optics—detector to several millimeters. In the optimal case, the spot size from an individual channel on the detector is equal approximately to the pixel size of $48\text{ }\mu\text{m}$.

Individual channels of the optics can guide fluorescence radiation to the detector by means of total reflection practically without losses. This effect allows increasing the intensity in comparison to a simple pinhole, however at the cost of additional beam spreading. The angle of the total reflection is equal to several milliradians, so that this additional spreading can be kept at the level of several micrometers at small distances of sample—optics and optics—detector. Furthermore, the polycapillary optics are free from the above-mentioned image distortion typical for a pinhole.

Conical polycapillary optics can be used for magnification or reduction of the image size.¹⁵ The magnification or reduction factors of 10 are quite realistic under the actual fabrication technology. In the camera, the exit diameters of the channels should be adapted to the pixel size of the detector in the same way as for a straight polycapillary. In particular, this means that a $10\times$ magnification optics can image a $5\text{ }\mu\text{m}$ region onto a single pixel, giving the spatial resolution of approximately $5\text{ }\mu\text{m}$ with the color camera under consideration.

The X-ray color camera uses parallel¹⁶ or conical¹⁵ polycapillary structures. The optics housings and the camera head are connected via a fine screw thread to the entrance window of the camera. The first results with the parallel polycapillary structures are presented and discussed below. Measurements with the conical structures are under survey.

Data Analysis. A dedicated user software was programmed for the camera. It controls the power supplies and the readout electronic system, monitors the house keeping sensors, analyzes the data, and displays and stores the resulting spectra cube. The software for the camera is written in C++ using the Qt¹⁷ and Qwt¹⁸ libraries. The event analysis part is based on XOnline.¹⁹ Because of the number of spectra (69 696) and the frame rate of 400 Hz, the frame analysis is optimized for analysis by multiple CPU cores. The representation of the data and the user interface is adopted for applications in real time spectral imaging.

In general, because of the thick sensitive volume, the charge cloud generated by X-rays with energies above 3 keV will spread along its drift path toward the front of the device. Hence, the charge signal of a single event will be recorded by multiple

neighboring pixels (split-event) without charge losses. The capability of a CCD to determine the number of generated electrons in every pixel allows event reconstruction algorithms to be applied in order to obtain the exact energy of the incoming photon. This is achieved by summing the contribution of all the neighboring pixels which recorded the event. The effectiveness of this method is limited only by the number of photons hitting the detector during the exposure time. If the photon count rate becomes too high, single event patterns will overlap; this prevents exact reconstruction of the energy and position information. If proper limitation of the incoming count rate is adopted (see section of First Measurement Results), a single photon energy spectrum can be recorded after event recombination.

As the position for split events is determined by the weighted position of several pixels, the center of impact of the photon is determined with subpixel accuracy.²⁰ The capacity of the subpixel analysis is under survey; thus far a minimum division of a pixel into four subpixels is possible. In this case, the size of the capillary has to be in the order of the aimed resolution.

The program acquires dark frames for calibration. From these, pixel wise offset and readout noise values are calculated. For illuminated frames the calculated offset is subtracted and the common mode effect is corrected for. Then each column is multiplied by a gain correction factor. This is necessary since each column corresponds to a different set of amplifiers. In the corrected image, each pixel with a signal higher than k times its readout noise is assumed to contain a real signal (k usually set to 4). Because of the presence of split-events, the image is then analyzed for neighboring pixels with signal. These groups of pixels are recombined to events. For each event, the total energy and position is calculated. Each event is then, according to its position, sorted into a 264×264 array which matches the pixel array on the chip.

Since the pnCCD is readout in two directions, events in the center of the image can be split as well. The recombination of these events by the software will be added in the future, thereby removing the dark stripe in the center of all shown images. The events are sorted into the spectra for each pixel so that a data cube with 69 696 spectra each of 2000 channels is accumulated in the course of time. This cube is further processed for the peak content of elements in each pixel and directly visualized. The data cube is obtained online and saved to the hard disk. One complete raw image (69 696 spectra with 2000 channel) takes 558 Byte of disk space for an intensity storage of 4 Byte per spectrum

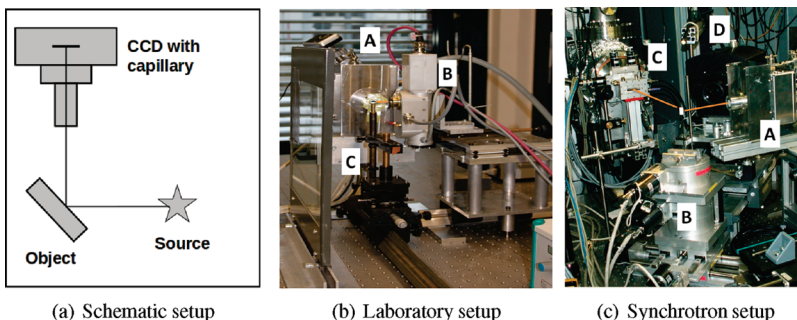


Figure 2. Setup for X-ray fluorescence measurements with a source–object–camera geometry of 45°/45°. (a) Schematic setup. (b) Laboratory setup: A, CXC; B, Rh-microfocus tube; C, sample holder. (c) Synchrotron setup: A, CXC; B, sample stage; C, exit of the synchrotron beam; D, microscope. The X-ray beam is indicated in orange.

channel, uncompressed. Compressing algorithms work effectively, and the reduction depends on the count distribution in the spectra.

Fast imaging of the elements is done by summing the number of counts in energy regions for the elemental fluorescence lines (regions of interest (ROIs)). These counts are mapped to a color scale and printed for each pixel to give an image of the elemental distribution of the sample. More elaborate offline analysis (including fitting of the fluorescence lines, taking a background and other effects into account) has to be done using standard XRF programs.

In this paper, we only show the fast imaging pictures. An example is shown in Figure 1. The fluorescence signal of three gold meshes excited with a Rh-microfocus tube are shown by selecting an energy region around the gold L-peak at 9.713 keV. The picture was taken with 50 μm 1:1 polycapillary optics, and the measuring time was 20 min. The meshes are supported by gold rings with a diameter of 3 mm, but due to a source–sample–camera geometry of 45°/45° the rings appear elliptical. As one can see at mesh b, a resolution of 50 μm is achieved. In Figure 1b, three pixel spectra are compared, one from the gold ring, one from the gold bar, and one in the hole of the mesh.

RESULTS

First Measurement Results. The characteristic data of the color X-ray camera, such as the maximum count rate, the spectral resolution, and the pixel homogeneity, were measured in the special test experiments. The pnCCD was operated at $T = -26\text{ }^{\circ}\text{C}$ with a deviation of $\Delta T = \pm 0.2\text{ }^{\circ}\text{C}$ and the pressure was $p \leq 4 \times 10^{-3}\text{ mbar}$.

If not stated differently, the following applications were performed with the following setup. The camera had a 1:1 polycapillary optics of 30.5 mm length, 50 μm capillary diameter, and 21.5 mm diameter for the capillary bundle. Two types of sources were used, a microfocus rhodium tube with a focal spot size of $0.05 \times 0.05\text{ mm}^2$, a 0.1 mm beryllium window, a maximum operating power of 30, and the synchrotron radiation from the BAMline facility at BESSY II.^{21–23} Imaging was performed by selecting regions of interest and color coding the intensities. The setup was a source–sample–camera geometry of 45°/45° (Figure 2a). The distances were optimized for the best count rates at the various samples. In Figure 2, the experimental setup in the laboratory (Figure 2b) and at the synchrotron (Figure 2c) are shown.

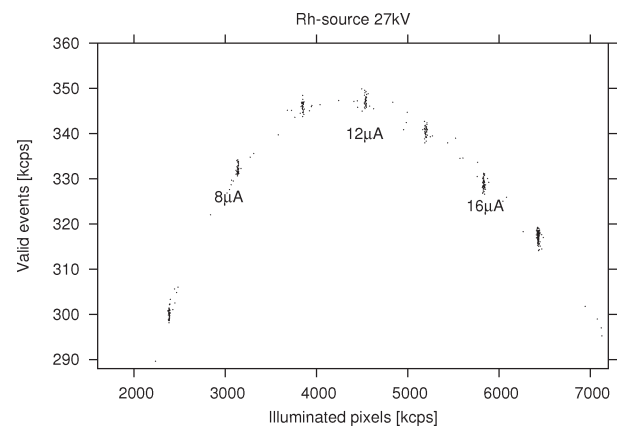


Figure 3. Valid events as a function of the illuminated pixels. The source is a 30 W rhodium microfocus tube. The CCD is fully illuminated by the microfocus tube.

The examples demonstrate the fast imaging capabilities of the camera. For exact quantitative statements, longer accumulation times are necessary as well as background corrections and final spectrum analysis.

Count Rates. The correct event reconstruction in terms of energy and position is the limiting factor for the maximum number of photons that can be detected on a frame. If there are too many incoming photons, the event patterns overlap and can therefore not be separated into real events representing real photons. The information about energy and position of these photons is lost. The typical pattern size distribution of the events is as follows: single 1.1%, double 19.2%, triple 32.2%, quadruple 43.6%, and quintuple 2.6%. Higher tuples up to eight are taken into account in the event analysis, but they amount to less than 1% in total.

Most of the events occupy 3–4 pixels plus 12 empty pixels all around. In Figure 3, an example of the rate of valid events as a function of the illuminated pixels is shown. A microfocus 30 W rhodium X-ray tube was used at a fixed voltage of 27 kV. The current was increased in steps of 2 μA, and the number of illuminated pixels and valid events were measured directly without any optics.

Illuminating the full frame, the maximum count rate obtained with the microfocus tube was below 350 kcps. For monochromatic synchrotron radiation of 13 keV at the BAMline facility, BESSY, a count rate of 450 kcps was achieved (not shown).

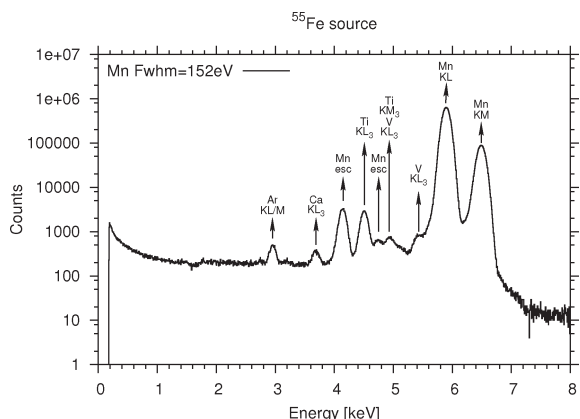


Figure 4. Sum spectrum of all pixels of a ^{55}Fe source, including scattering light from the surrounding environment.

Much higher count rates are possible if one sets aside the event analysis. The camera is not working as a single photon counter but detects the total energy delivered on the chip. In the case of a single hit of each pixel and split events over 4 pixels, the rate of photons is $264 \times 164 \times 400/4 = 6969\text{kcps}$. If the ADC range is larger than the photon energy, each pixel can be hit more than once, increasing the count rate.

Spectral Resolution. The spectral resolution was determined using a ^{55}Fe source in front of the camera and measuring the K_α line of manganese at a count rate of 340 kcps. The sum spectrum of all pixels was fitted using the PyMCA²⁴ code giving a spectral resolution of the total spectrum (sum of all pixel spectra) of 152 eV for Mn K_α at 5898.75 eV (see Figure 4).

In the spectrum, the argon peak from air and additional peaks from calcium, titanium, and vanadium, which are caused by scattered radiation from the surroundings, are visible.

Pixel Homogeneity. The homogeneity of the response of each pixel was estimated by measuring the fluorescence of a manganese foil excited by 17 keV monochromatic synchrotron radiation. Events were recorded until each illuminated pixel had at least 10 000 events. A ROI around the manganese lines was set, and the counts for each pixel in the ROI were determined. The number of manganese counts in the spectra was around 94% while 6% of the counts are scattering light from the surrounding environment. The standard deviation of the pixel counts for each CAMEX region and for the total region, excluding the borders, was calculated.

Borders were set in order to avoid taking into account unilluminated pixels and pixels on the CAMEX borders (a separation between the CAMEX is introduced, too). The two top CAMEX have a mean count value of 9348 with a σ of 457 and 484, that is 4.9% and 5.2%, respectively. The lower left CAMEX has 9280 counts with a σ of 423 (4.6%), the lower right one has 9348 counts with a σ of 451 (4.8%). Assuming a Poisson counting statistic, at 10 000 counts a σ of 100 (1%) is obtained. The significant enhanced inhomogeneity compared to the pure Poisson statistic could be due to additional statistics from the event analysis and is the subject of ongoing investigations.

First Pictures with the Microfocus Source. One example with a rhodium tube is presented. A red-toothed shrew (*Sorex*), which was approximately 1 cm² in size, was investigated with the CXC. The teeth of the shrew are hardened by iron oxide, which is shown in Figure 5, where the iron distribution is shown in red

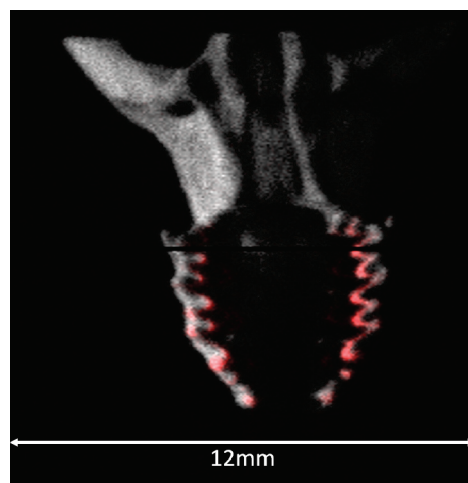


Figure 5. Distribution of calcium (gray) and iron (red) in the skull of a red-toothed shrew, *Sorex araneus* (ZMB 61372). Exposure time is 1 h.

and the calcium distribution in gray. The exposure time was 1 h, the distance source-object was 2 cm, and the distance object-polycapillary was 1 cm. The first impression of the skull and the teeth was visible after 5 min.

First Pictures with Synchrotron Radiation. First experiments with synchrotron radiation showed that the camera is well suited for art analysis. A ceramic fragment from Lisbon is shown in Figure 6 on the left side (Figure 6a), the section analyzed by the camera is indicated by the orange square. On the right side (Figure 6b), the corresponding RGB image is presented, with the Fe distribution in green, Mn in red, and Ca in blue. The measurement time for the image was 30 min.

SUMMARY AND OUTLOOK

In collaboration with the Institute for Scientific Instruments GmbH, the Federal Institute for Materials Research and Testing, the Institut für Angewandte Photonik e.V., and PNSensor GmbH, the first prototype of a color X-ray camera was set up and tested. The first measurements with synchrotron radiation and with a Rh-microfocus tube showed that the CXC is a high quantum efficiency, high-speed detector for spatial and energy resolved X-ray detection, in particular for XRF imaging applications.

The camera measures a total of 69 696 spectra, simultaneously. The overall count rate is a maximum of 450 kcps, and the image area has a size of about 1 cm². The spectral resolution is 152 eV for Mn K_α at -26 °C chip temperature. A spatial resolution of 48 μm was obtained due to the polycapillary optics. A software updates the sums of the counts for certain energy channel ranges during the measurement and displays 2-D false-color maps as well as sumspectra of selected regions.

Because of the combination of spatial and spectral analysis, several interactions of the X-ray beam with matter, such as absorption, excitation, total reflection, and scattering can be measured in two dimensions. Therefore, without the need of stepwise mapping of a sample, the characterization of objects of various elemental components is significantly enhanced. For computerized X-ray tomography (CT), the camera in combination with conventional (nonenergy resolved) CT adds valuable information on the elemental composition. If lower spatial resolution is acceptable, element selective tomography can be

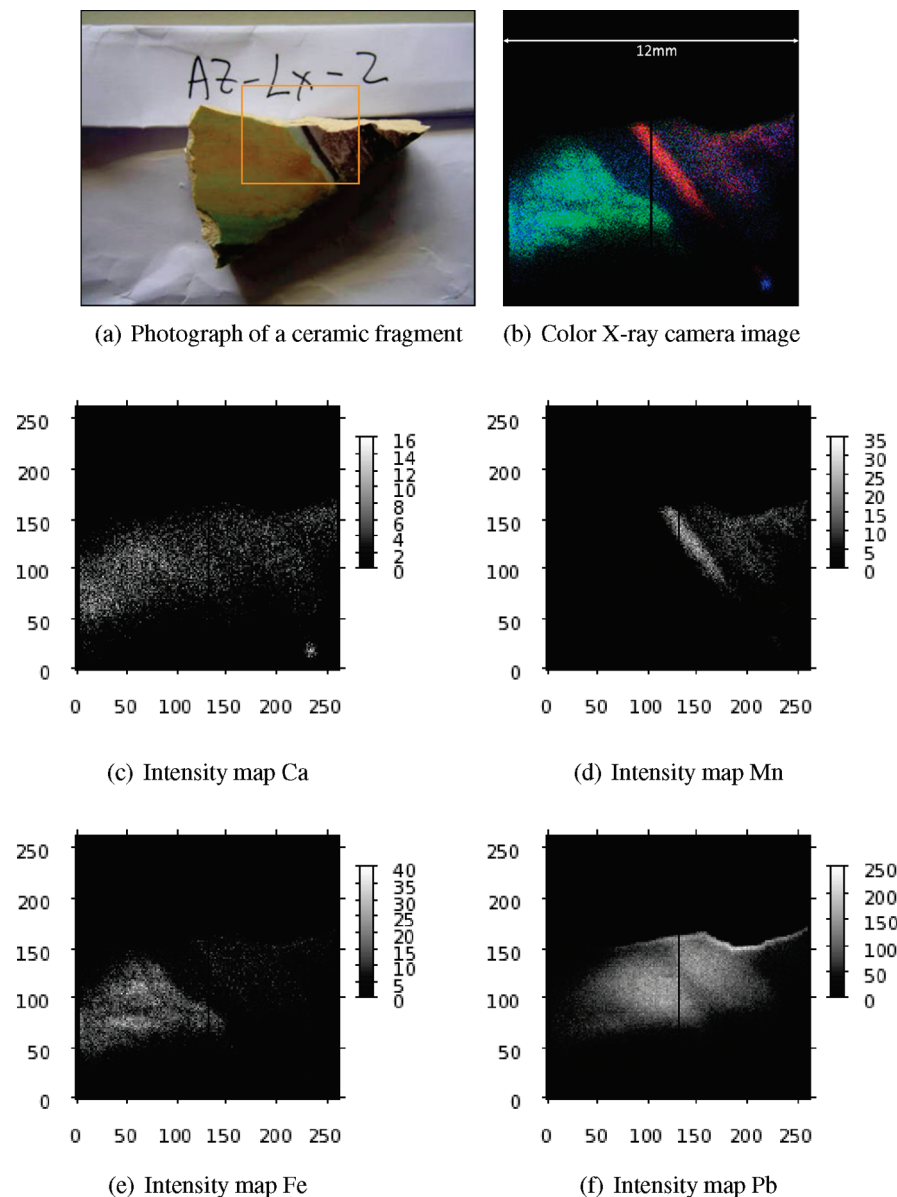


Figure 6. Ceramic fragment (AZ-LX-2) from Lisbon (courtesy of A. Guilherme Buzanich). (a) Photograph of a ceramic fragment with the analyzed part by the CXC indicated by the orange square. (b) Color X-ray camera image of a part of the ceramic fragment. The Fe distribution is in green, Mn in red, and Ca in blue. Intensity maps, representing the sum of counts in selected ROIs for (c) Ca, (d) Mn, (e) Fe, and (f) Pb.

performed with this camera. With X-ray absorption near edge spectroscopy (XANES), the CXC offers the possibility of also obtaining spatially resolved chemical information of an elemental distribution (coordination environment, oxidation states). We had hoped to find different oxidation states in the Sorex teeth but have had no success thus far. The diffraction patterns obtained by XRD analysis proved additional information on the lattice orientation in parts of the sample, in addition to the fluorescence lines. Other applications as total reflection X-ray fluorescence (TXRF) and grazing exit X-ray absorption fluorescence (GEXAF) are under survey.

The future developments for the camera setup aim at a true tabletop device with no pump and cooling water as well as more compact electronics. If higher frame rates are achieved, higher count rates become possible and a thinner window will allow to measure light elements as well.

■ AUTHOR INFORMATION

Corresponding Author

*E-mail: scharf@ifg-adlershof.de.

■ ACKNOWLEDGMENT

We would like to thank Frieder Mayer (Museum für Naturkunde Berlin) for providing the specimen of the common shrew *Sorex araneus* (ZMB 61372) and Peter Giere (Museum für Naturkunde Berlin), who in cooperation with Markus Kühbacher studied the composition of the teeth in common shrews. Thanks also to Ana Guilherme Buzanich (Atomic Physics Centre, University of Lisbon) for the ceramic fragment (AZ-LX-2) from Lisbon. This project is partially financed by the Land Berlin within the framework of the program ProFIT

(Project Numbers 10139911, 10139913, and 10139914) and cofinanced by the European Union (European Regional Development Fund).

■ REFERENCES

- (1) Burkhard, B.; Kanngießer, B.; Langhoff, N.; Wedell, R.; Wolff, H. *Handbook of Practical X-Ray Fluorescence Analysis*; Springer: New York, 2006; pp 85–284.
- (2) Janssens, K. H. A.; Adams, F. C. V.; Rindby, A. *Microscopic X-ray Fluorescence Analysis*; John Wiley and Sons, 2000.
- (3) Alfeld, M.; Janssens, K.; Liu, X.; Kostenko, A.; Rickers-Appel, K.; Falkenberg, G. *AIP Conf. Proc.* **2010**, 1221 (1), 111–118.
- (4) Meidinger, N. *SPIE 2009*, 7435, 743502.
- (5) Bjeoumikhov, A.; Langhoff, N.; Wedell, R.; Beloglazov, V.; Lebedev, N.; Skibina, N. *X-ray Spectrom.* **2003**, 32, 172–178.
- (6) Strüder, L.; Briel, U.; Dennerl, K.; Hartmann, R.; Kendziorra, E.; Meidinger, M.; Pfeffermann, E.; Reppin, C.; Aschenbach, B.; Bornemann, W.; Bräuninger, H.; Burkert, W.; Elender, M.; Freyberg, M.; Haberl, F.; Hartner, G.; Heuschmann, F.; Hippmann, H.; Kastelic, E.; Kemmer, S.; Kettenring, G.; Kink, W.; Krause, N.; Müller, S.; Oppitz, A.; Pietsch, W.; Popp, M.; Predehl, P.; Read, A.; Stephan, K. H.; Stötter, D.; Trümper, J.; Holl, P.; Kemmer, J.; Soltau, H.; Stötter, R.; Weber, U.; Weichert, U.; von Zanthier, C.; Carathanassis, D.; Lutz, G.; Richter, R. H.; Solc, P.; Böttcher, H.; Kuster, M.; Staubert, R.; Abbey, A.; Holland, A.; Turner, M.; Balasini, M.; Bignami, G. F.; La Palombara, N.; Villa, G.; Buttler, W.; Gianini, F.; Lainé, R.; Lumb, D.; Dhez, P. *Astronom. Astrophys.* **2001**, 365, 18–26.
- (7) Strüder, L.; Bräuninger, H.; Briel, U.; Hartmann, R.; Hartner, G.; Hauff, D.; Krause, N.; Maier, B.; Meidinger, N.; Pfeffermann, E.; Popp, M.; Reppin, C.; Richter, R.; Stötter, D.; Trümper, J.; Weber, U.; Holl, P.; Kemmer, J.; Soltau, H.; Viehl, A.; Zanthier, C. *Rev. Sci. Instrum.* **1997**, 68, 4271–4274.
- (8) Hofäss, H.; Vetter, U.; Ronning, C.; Uhrmacher, M.; Bharuth-Ram, K.; Hartmann, R.; Strüder, L. *Nucl. Instrum. Methods Phys. Res., Sect. A* **2003**, 512, 378–385.
- (9) Leitenberger, W.; Hartmann, R.; Andritschke, R.; Starke, I.; Strüder, L. *J. Synchrotron Radiat.* **2008**, 15, 449–457.
- (10) Strüder, L.; Epp, S.; Rolles, D.; Hartmann, R.; Holl, P.; Lutz, G.; Soltau, H.; Eckart, R.; Reich, C.; Heinzinger, K.; Thamm, C.; Rudenko, A.; Krasniqi, F.; Kühnel, K.-U.; Bauer, C.; Schröter, C.-D.; Moshammer, R.; Techert, S.; Miessner, D.; Porro, M.; Häcker, O.; Meidinger, N.; Kimmel, N.; Andritschke, R.; Schopper, F.; Weidenspointer, G.; Ziegler, A.; Pietschner, D.; Herrmann, S.; Pietsch, U.; Walenta, A.; Leitenberger, W.; Bostedt, C.; Möller, T.; Rupp, D.; Adolph, M.; Graafsma, H.; Hirsemann, H.; Gärtnner, K.; Richter, R.; Foucar, L.; Shoeman, R.; Schichtling, I.; Ullrich, J. *Nucl. Instrum. Methods Phys. Res., Sect. A* **2010**, 614 (3), 483–496.
- (11) Gatti, E.; Rehak, P. *Nucl. Instrum. Methods Phys. Res., Sect. A* **1984**, 225, 608–614.
- (12) Hermann, S.; Buttler, W.; Hartmann, R.; Meidinger, N.; Porro, M.; Strüder, L. In *IEEE Conference Records*; 2008; pp 2952–2957.
- (13) Zschornack, G. *Handbook of X-ray Data*; Springer: Berlin, Germany, 2007.
- (14) Ordavo, I.; Ihle, S.; Gubzhokov, R.; Arkadiev, V.; Scharf, O.; Bjeoumikhov, A.; Bjeoumikhova, S.; Buzanich, G.; Gubzhokov, R.; Günther, A.; Hartmann, R.; Lang, M.; Langhoff, N.; Liebel, A.; Radtke, M.; Reinholz, U.; Riesemeier, H.; Soltau, H.; Strüder, L.; Wedell, R. *Nucl. Instrum. Methods Phys. Res., Sect. A* **2011**, Submitted.
- (15) Bzhaumikhov, A. A.; Langhoff, N.; Schmalz, J.; Wedell, R.; Beloglazov, V. I.; Lebedev, N. F. *Proc. SPIE* **1998**, 3444, 430–435.
- (16) Arkadiev, A. A.; Bzhaumikhov, A. A. *Proc. SPIE* **1995**, 2515, 514–525.
- (17) Trolltech, Qt graphical library, 2010, www.trolltech.com.
- (18) Rathmann, U. Qwt graphical library, 2010, qwt.sourceforge.net.
- (19) Kimmel, N.; Holl, P. Online; 2009, Driver and analysis software for pnCCDs.
- (20) Kimmel, N. Ph.D. Thesis, Universität Siegen, Siegen, Germany, 2009.
- (21) Riesemeier, H.; Ecker, K.; Görner, W.; Müller, B.; Radtke, M.; Krumrey, M. *X-Ray Spectrom.* **2005**, 34, 160–163.
- (22) Strub, E.; Plarre, R.; Radtke, M.; Reinholz, U.; Riesemeier, H.; Schoknecht, U.; Urban, K.; Jüngel, P. *Nucl. Instrum. Methods Phys. Res., Sect. B* **2008**, 266, 2405–2407.
- (23) Simons, C.; Mans, C.; Hanning, S.; Jan, A.; Radtke, M.; Reinholz, U.; Ostermann, M.; Michaelis, M.; Wienold, J.; Alber, D.; Kreyenschmidt, M. *J. Anal. At. Spectrom.* **2010**, 25, 40–43.
- (24) Solé, V. A.; Papillon, E.; Cotte, M.; Walter, P.; Susini, J. *Spectrochim. Acta, Part B* **2007**, 62, 63–68.